

---

# Learning What's Real: Disentangling Signals from Measurement Artifacts in Multi-Sensor Data, with Applications to Astrophysics

---

**Pablo Mercader-Perez**

Massachusetts Institute of Technology  
pablomer@mit.edu

**Carolina Cuesta-Lazaro**

Flatiron Institute, Simons Foundation  
Institute for Advanced Studies  
cuestalz@mit.edu

**Daniel Muthukrishna**

Massachusetts Institute of Technology  
AstroAI, CfA | Harvard & Smithsonian  
danmuth@mit.edu

**Jeroen Audenaert**

Massachusetts Institute of Technology  
jeroena@mit.edu

**V. Ashley Villar**

Harvard University  
The NSF IAIFI  
ashleyvillar@cfa.harvard.edu

**David W. Hogg**

New York University  
Flatiron Institute, Simons Foundation  
david.hogg@nyu.edu

**Marc Huertas-Company**

Instituto de Astrofísica de Canarias  
mhuertas@iac.es

**William T. Freeman**

Massachusetts Institute of Technology  
billf@mit.edu

## Abstract

Data collected from the physical world is always a combination of multiple sources: an underlying signal from the physical process of interest and a signal from measurement-dependent artifacts from the sensor or instrument. This secondary signal acts as a confounding factor, limiting our ability to extract information about the underlying physics. Moreover, it poses significant challenges for combining data in heterogeneous or multi-instrument frameworks. To disentangle these factors of variation, we propose a dual-encoder architecture with a counterfactual generation objective that leverages overlapping observations. The resulting representations explicitly separate intrinsic signals from sensor-specific distortions and noise, and can be used for counterfactual view generation, parameter inference, and instrument-independent similarity search—all unconfounded by measurement artifacts. We demonstrate the effectiveness of our approach in a multi-instrument setting on astrophysical galaxy images from the DESI Legacy Imaging Survey (Legacy) and the Hyper Suprime-Cam (HSC) Survey. This framework provides a general recipe for scientific self-supervised pretraining: construct training pairs from overlapping observations of the same physical system, treat sensor- or modality-specific effects as augmentations, and learn invariant representations through counterfactual generation.

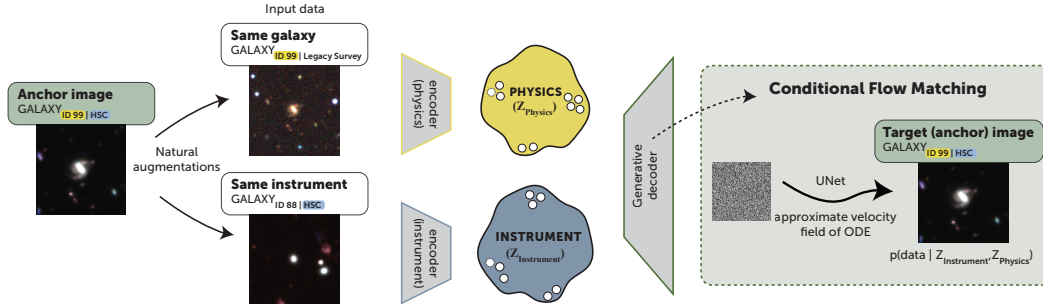


Figure 1: **Counterfactual Reconstruction.** The model learns to disentangle intrinsic galaxy properties from instrument systematics by reconstructing an anchor image. Training uses **data triplets**: an **anchor observation** (signal  $s$  from instrument  $i$ ), an instrument-augmented observation (**same source**  $s$ , a different instrument  $i'$ ), and a physics-augmented observation (a different source  $s'$ , **same instrument**  $i$ ). The *physics* encoder extracts latents from the instrument-augmented pair to capture invariant physical features, while the *instrument* encoder processes the physics-augmented observation to isolate measurement artifacts. These latent variables jointly condition the flow-matching decoder. Crucially, the anchor image is never fed into the encoders; it is used only as a target for the flow-matching loss, forcing the model to generate the reconstruction counterfactually.

## 1 Introduction

Observational data collected from the physical world can be viewed as the result of a causal process. First, an event of interest occurs, generating a physical signal. For example, a distant pulsating star emits electromagnetic waves, a person speaking creates pressure waves in the air, and a beating heart produces pressure waves that propagate through blood vessels. This signal cannot be directly observed. Instead, it must pass through a sensor or instrument that records it. Any instrument used introduces measurement artifacts, often referred to as *instrument systematics* or bias. These effects include transformations like the nonlinearity of Charge-Coupled Devices (CCD) in a camera or a microphone’s frequency response. These act as *confounding* factors. However, with sufficient understanding of the measurement system, they can often be partially modeled and disentangled from the underlying signal. Additionally, stochastic noise imposes a limit on measurement precision.

In other words,  $Observation = f(Signal, Instrument) + Noise$ . In some cases,  $f$  is relatively simple, such as a point-spread function (PSF) convolution that only requires accurate characterization of the optics. However, it often cannot be modeled fully analytically. The true signal is explained by variables that are independent of the measurement and contain the scientifically relevant information; we refer to these as **physics variables**. The instrumental effects arise from measurement distortions and act as confounders; we refer to these as **instrument variables**.

We present a general approach to disentangle physics and instrument variables when the same system is observed by multiple instruments. The key insight is that cross-matched observations form natural pairs of *same physics, different instrument*, providing a training signal for separating the two sets of factors without requiring an explicit forward model of either instrument.

We demonstrate our approach on astrophysical galaxy images, a domain where modeling instrument systematics is critical. Photons emitted by a distant source must traverse cosmic dust and the Earth’s atmosphere before being recorded by ground-based telescopes, each with its own optics, detector characteristics, and observing conditions. As a result, the same galaxy can look remarkably different across two telescopes due to differences in resolution, noise, and calibration. Historically, obtaining observations of the same phenomena with multiple instruments has been essential for distinguishing real physical signals from instrumental artifacts. For example, gravitational waves signals require confirmation by multiple detectors because the signal is buried deep in detector noise. In this work, we train our model on  $\sim 100,000$  cross-matched galaxy images from two different ground-based telescopes and show that we learn disentangled representations separating the intrinsic properties of galaxies from the instrument-specific effects, enabling robust inference of galaxy properties, outlier detection, counterfactual generation across instruments, and instrument-independent similarity search.

## 2 Related work

**Disentangled representation learning.** Learning representations that separate independent factors of variation is a longstanding goal in representation learning. Tenenbaum and Freeman [1] explored bilinear representations to separate style and content. Early work on variational autoencoders (VAEs), such as  $\beta$ -VAE [2], encouraged disentanglement by regularizing the latent space via the loss function. A natural source of structure is multi-view observations, where the same underlying content is observed under varying conditions or at different times. From a causal perspective, Schölkopf et al. [3] framed disentanglement as the recovery of independent causal mechanisms, connecting representation learning and causal inference. Our framework draws on these ideas but enforces structural disentanglement through a specific architecture-driven information bottleneck and a counterfactual generation objective, rather than relying on hand-engineered loss functions.

**Foundation models in the Sciences.** Pre-training self-supervised representations on large scientific datasets has recently seen success in different areas of science like biology [e.g., 4, 5] and satellite imagery [e.g., 6]. In astrophysics, Walmsley et al. [7] demonstrated the value of self-supervised representations for downstream tasks. More recently, Parker et al. [8] developed AION-1, a large-scale foundation model trained via masked modeling across modalities such as imaging and spectra from the Multimodal Universe dataset [9]. However, a limitation common to these approaches is that instrument-specific effects are either ignored or treated as independent modalities without explicit disentanglement. This has practical consequences for downstream tasks. For instance, a model developed for ESA’s Euclid mission [10] found that instrument systematics, rather than physically interesting sources, dominated the outliers identified in the latent space. Our work addresses this by building the separation of physics and instrument factors into the architecture itself.

**Incorporating multi-instrument observations in Foundation Models.** Recently in astrophysics, Audenaert et al. [11] leveraged the causal representation ideas from Schölkopf et al. [12, 3], Hattori et al. [13], to causally separate astrophysical observations into a physics and instrument component by using a dual-encoder architecture. They used a dataset of simulated astronomical time series captured by multiple instruments to learn a *physics latent space* that encodes information about the target star and an *instrument latent space* that encodes information about the measurement configuration. This is achieved by leveraging triplets of overlapping observations and using contrastive learning. While effective, contrastive objectives have inherent limitations for our setting. By aligning representations across views of the same source, they tend to retain only the information shared across all views, effectively collapsing toward the lowest-resolution observation in the set and discarding fine-grained features that are visible in higher-quality instruments. Also importantly, contrastive embeddings are not optimized for pixel-level reconstruction and producing counterfactual views would require training a separate generative model on the learned embeddings, with no guarantee that the necessary information is preserved. Our generative objective addresses these limitations.

## 3 Methods

We present a counterfactual generation objective designed to learn representations that disentangle physical properties from measurement systematics. Our goal is to capture robust physical information into a physics latent space, while learning a data-driven noise model for each of the instruments.

**Counterfactual Generative Objective.** Our framework leverages large-scale scientific datasets with overlapping observations from multiple instruments. In this setting, natural augmentations can be used to construct triplets: an anchor, an observation of the same source (but different instrument), and an observation on the same instrument (but different source), as shown in Fig. 1.

A *physics encoder* receives a sample from the target source but from a different instrument, so it is encouraged to reduce the loss by capturing the underlying physical properties of the source and becoming invariant to the instrumental distortions. Similarly, an *instrument encoder* receives a sample from the target instrument but a different source, so it is encouraged to capture instrument-specific distortions while ignoring the content specific to the source. The decoder combines these two latent embeddings to reconstruct an unseen target or anchor observation.

Formally, consider a set of  $N$  sources observed across  $M$  instruments, where  $x_{j,k}$  denotes the observation of source  $j$  as captured by instrument  $k$ . We aim to learn the conditional distribution  $p(x_{j,k} \mid \{z_{\text{phy}}(x_{j,k'})\}_{k' \neq k}, \{z_{\text{ins}}(x_{j',k})\}_{j' \neq j})$ , for all source–instrument pairs  $(j, k)$ . Here

$\{z_{\text{phy}}(x_{j,k'})\}_{k' \neq k}$  are the physics embeddings extracted from observations of the *same source*  $j$  by *other instruments*  $k' \neq k$ , which provide information about the source’s intrinsic physical properties. The set  $\{z_{\text{ins}}(x_{j',k})\}_{j' \neq j}$  are the instrument embeddings extracted from observations of *other sources*  $j'$  by the *same instrument*  $k$ . This formulation allows the model to leverage all available multi-instrument data: the physics of the target source is informed by its appearances across different instruments, while the instrument response is informed by how other sources appear under similar observing conditions. Note that the number of source and instrument neighbors may vary; therefore, we combine the variable sequence of embeddings via attention-based conditioning.

We model this conditional distribution using flow matching [14], learning a velocity field  $u_{\theta}(x, t, z_{\text{phy}}, z_{\text{ins}})$  that transports samples from Gaussian base distribution to the target distribution. The training loss is given by the error on the predicted velocity field,

$$\mathcal{L}_{\text{FM}}(\theta) = \mathbb{E}_{\substack{t \sim \mathcal{U}[0,1] \\ j \sim [N], k \sim [M] \\ x_{j,k} \sim \mathcal{P}^{\text{data}} \\ x_0 \sim \mathcal{N}(0, I)}} \left[ \left\| u_{\theta}(x_t, t, \{z_{\text{phy}}(x_{j,k'})\}_{k' \neq k}, \{z_{\text{ins}}(x_{j',k})\}_{j' \neq j}) - (x_{j,k} - x_0) \right\|^2 \right] \quad (1)$$

where  $x_t = (1-t)x_0 + tx_{j,k}$ . That is, we sample a source  $j$ , a target instrument  $k$ , a noise sample  $x_0$ , and a timestep  $t$ , and train the velocity field to reconstruct the observation  $x_{j,k}$  from a noisy state  $x_t$  conditioned on physics latents from other instruments and instrument latents from different sources.

Once trained, the physics embedding supports downstream tasks such as outlier detection, parameter inference, classification, or embedding-based retrieval, while the instrument space allows to find similar systematics and observing conditions. The generative decoder enables generating counterfactual views. In astrophysics, a particularly promising use case is to inform follow-up observations by predicting high-resolution observations from expensive facilities using low resolution observations from a different instrument.

## 4 Application to Astrophysics: Galaxy foundation models

Datasets in astrophysics have grown considerably over the last decade. In particular, galaxy surveys such as DESI, have now imaged over a billion galaxies while taking spectra of over 10 million galaxies. This has sparked interest in developing foundation models for galaxies that learn semantic representations of astronomical data, helping us search large databases, identify interesting anomalies, and predict galaxy properties of interest. Up to now, these models have treated data from different instruments as independent modalities [8]. Here, we show that counterfactual reconstruction improves robustness to instrument systematics while enabling new foundational capabilities, including cross-instrument generation, instrument-independent retrieval, and data-driven denoising.

We take a cross-matched dataset from the Multimodal Universe that includes  $\sim 100,000$  cross-matched galaxy images from the DESI Legacy Imaging Surveys [Legacy, 15] and the Hyper Suprime-Cam [HSC, 16] survey as a representative multi-instrument setting. HSC is a deeper and higher-resolution instrument that can detect significantly fainter features that would otherwise be masked by noise in Legacy. However, by making this compromise, Legacy covers a larger area of the sky,  $\approx 20,000 \text{ deg}^2$ , compared to HSC,  $\approx 1,200 \text{ deg}^2$ , resulting in a trade-off between coverage and signal-to-noise.

**Data Preprocessing.** We have two sets of heterogeneous flux measurements: HSC provides five color filters with discrete wavelength bands ( $g, r, i, z, y$ ), and the Legacy Survey uses four ( $g, r, i, z$ ). Despite the shared designations, they differ significantly in their central wavelengths, pixel scales, zero-points, and noise characteristics. Our preprocessing pipeline follows the strategy established by [8], with one key difference: rather than treating all nine bands as distinct channels, we align the overlapping ( $g, r, i, z$ ) filters across both surveys into a unified four-channel representation and treat both sources as the same modality. For this purpose, we discard the additional HSC  $y$ -band channel, but future work could incorporate it.

Following [8], we normalize the zero-points by rescaling HSC measurements to the Legacy standard of 22.5 mag using the relation:  $s = 10^{(ZP-22.5)/2.5}$ . Then, we apply an arcsinh normalization to handle the images’ large dynamic range. Finally, we crop the HSC images into  $48 \times 48$  pixel cutouts. To account for the differing pixel scales between surveys ( $0.168''$  for HSC vs.  $0.262''$  for Legacy), we extract the inner  $31 \times 31$  pixels of the Legacy images and upsample them to  $48 \times 48$  pixels via linear interpolation; this ensures spatial alignment and a consistent field of view across pairs.

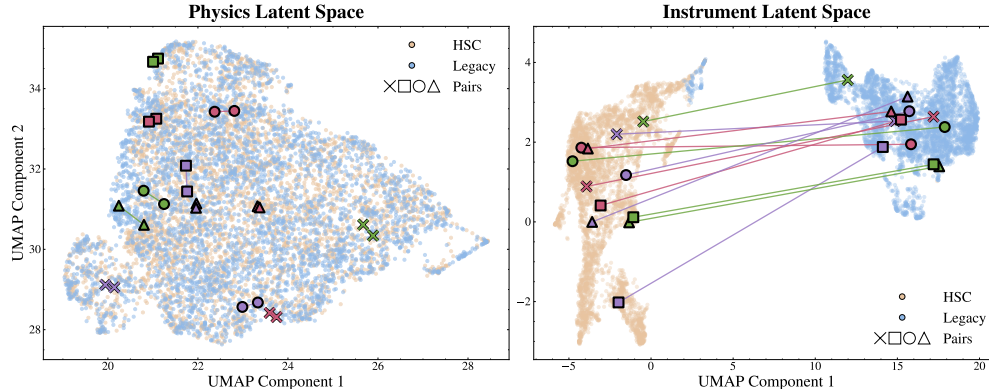


Figure 2: **Disentanglement.** UMAP projections of the physics (left) and instrument (right) latent spaces. Orange and blue points represent HSC and Legacy images, respectively. Matched markers ( $\Delta$ ,  $\times$ ,  $\square$ ,  $\circ$ ) denote cross-survey pairs. In the *physics space*, the encoders produce overlapping distributions where cross-survey pairs are mapped to similar coordinates. In contrast, the *instrument space* shows a clean separation between surveys and pairs, confirming that this space captures survey-specific features rather than intrinsic galaxy properties.

**Data Triplets.** In this dual-survey setting, each data point has a unique galaxy pair, providing the physics-augmented view. For the instrument views, we condition on up to five images of different galaxies observed by the same survey as the anchor. We select these as the five nearest spatial neighbors in the given survey within an angular separation of 3 arcminutes. This choice is motivated by the fact that instrumental systematics - such as PSF size and depth - vary smoothly across the sky, so spatially nearby observations share similar instrument conditions with the anchor.

**Model Implementation.** We use a modified ResNet-18 [17] for both encoders (physics and instrument) as described in Appendix A.1. We map each input image to a sequence of 4 spatial tokens of 16 dimensions, i.e. a latent representation of shape  $(B, 4, 16)$ . To accommodate a variable number of conditioning examples, we treat these embeddings as a set of tokens. For a given input set, the tokens from all images are concatenated into a single sequence of variable length. Then, we use cross-attention layers within our velocity network, a UNet2DConditionModel [18]. This allows the model to leverage an arbitrary number of context image embeddings during the generative process.

#### 4.1 Disentangled representations

First, we demonstrate that the physics and instrument latent spaces do show the expected disentanglement. We encode 8,192 image pairs from HSC and Legacy Surveys using both the physics and instrument encoders, and visualize the resulting latent embeddings using a 2D UMAP projection [19] in Fig. 2. The latent space demonstrates a clear separation of information. In the instrument space, HSC and Legacy observations form two distinct clusters, confirming that the encoder successfully captures survey-specific characteristics. In the physics space, the two surveys have largely overlapping distributions, indicating that the encoder has learned an approximate domain-invariant representation of the underlying galaxy properties. The overlap is, however, not expected to be perfect since the two surveys provide different amounts of constraining power on the underlying physical properties. The emergence of alignment of pairs observed in Fig. 2 from the reconstruction objective alone confirms that the architectural bottleneck is sufficient to drive the convergence of physics representations across the two surveys.

**Outlier detection unconfounded by instrument systematics.** Naively learned representations often bias outlier detection toward rare instrument artifacts rather than physically interesting sources. Our disentangled representation addresses this by separating physics and instrument factors, enabling outlier detection separately in each latent space: rare astrophysical sources in the physics space and rare observing conditions in the instrument space.

We encode all  $\sim 100,000$  HSC galaxies using the physics encoder and the instrument encoder separately. As a baseline, we encode the same images with AION-1 [8], a foundation model that treats each survey as an independent modality without explicit disentanglement. For each of the three latent spaces, we fit a normalizing flow to the empirical distribution of embeddings and rank all

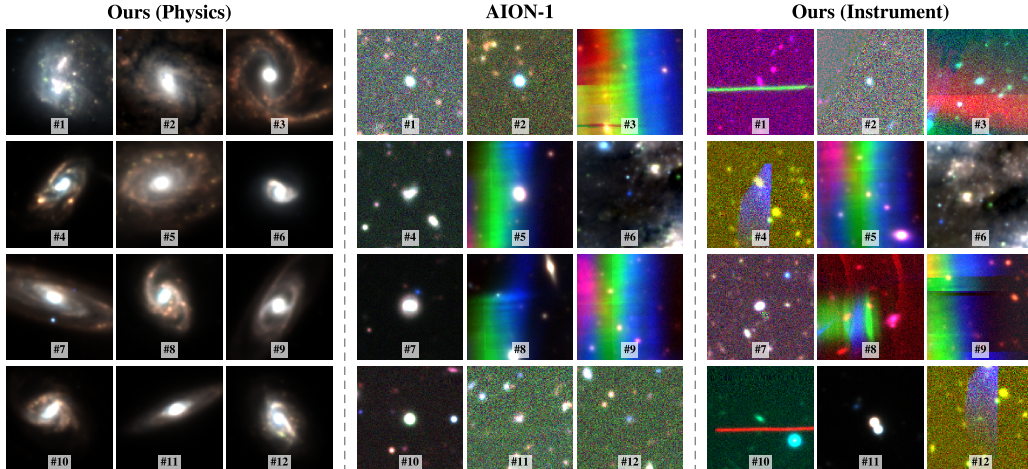


Figure 3: **Outlier Detection.** Top twelve outliers from each of the three latent spaces. **Left:** our physics latent reveals morphologically unusual sources (e.g., galaxy mergers), free of artifacts. **Middle & Right:** anomalies from AION-1 and our instrument latent are dominated by instrumental pathologies (saturated pixels, bands, noise patterns), confirming that our representation separates physical anomalies from instrument systematics.

sources by their estimated log-likelihood (Appendix A.7). The lowest-likelihood examples are the candidate outliers.

Fig. 3 shows the top twelve outliers from each latent space. The AION-1 anomalies contain several instrumental pathologies: saturated pixels from bright stars, vertical rainbow bands, and high-noise patterns. Outliers from our instrument space show similar characteristics, confirming that the instrument encoder captures systematics-related variation. In contrast, anomalies from our physics space are visibly free of these artifacts and reveal morphologically unusual sources: galaxy mergers, disturbed systems, and other candidate rare objects. We show cutouts at the full  $160 \times 160$  pixel size.

**Parameter inference robust to instrument systematics.** To evaluate the information content and disentanglement of our latent spaces, we train a small MLP (Appendix A.3) to predict physical and instrumental properties from embeddings extracted by each encoder on Legacy and HSC images. For the physics latent space we flatten across the token dimension; for the instrument latent space we apply mean pooling. In both cases, we concatenate the HSC and Legacy embeddings before feeding them into the MLP. We compare against AION-1 (Base) embeddings and against a randomly initialized, frozen ResNet-18 with the same architecture as our encoders. Fig. 4 shows the resulting regression  $R^2$  per property.

The physical properties of galaxies were inferred by Hahn et al. [20] from spectroscopic data, not from the images themselves, so they are only partially recoverable from imaging alone. Moreover, we note that these are not “physics only” properties. For instance, the galaxy’s redshift determines its apparent brightness, angular size, and observed colors—properties that are also changed by instrument conditions such as depth and PSF. Morphology is also affected by the instrument’s PSF. Therefore, the instrument encoder will inevitably retain some of this information. On the other hand, observing conditions, such as PSF size and depth, vary across each survey’s footprint as a function of sky position, determined by the tiling strategy and the atmospheric conditions during each field’s observation. Therefore, the physics latent space may retain some of this information. Details on the properties and source catalogs are provided in Appendix A.4.

The physics latent space recovers physical properties at a level comparable to AION-1. The randomly initialized ResNet serves as a reference for what an encoder of this architecture captures by default, purely from the inductive biases of the ResNet [21], without any training signal encouraging or discouraging it to encode specific information. Comparing our trained encoders to this baseline isolates what each latent space has actually been pushed to learn. Under this lens, the instrument latent space retains some information about physical properties, in particular redshift, stellar mass, and morphology. As explained above, this is expected to some degree, though we cannot quantify

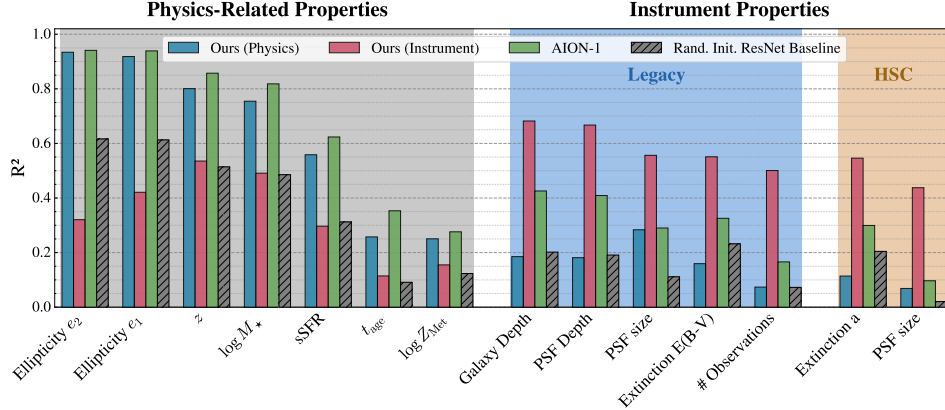


Figure 4: **Probing Latent Disentanglement via Downstream Regression.** We report  $R^2$  scores for the prediction of physics-related properties (left) and instrumental properties (right) on four sets of representations: our physics embeddings (blue), our instrument embeddings (red), AION-1 embeddings which treat each survey as an independent modality (green), and a randomly initialized ResNet-18 of the same architecture as our encoders (hatched black). We distinguish physics-related properties and instrument properties, which are grouped by survey. The asymmetry between the two panels demonstrates that our architecture successfully separates physics properties from instrument-specific information.

it. In the future, we will study how the capacity of the instrument bottleneck affects these results, especially given that the untrained ResNet exceeds our encoder’s predictive power on some properties.

To further disentangle genuine leakage of instrument into physics from shared spatial structure, we train a ResNet to predict each survey’s instrument properties directly from the other survey’s image ("Cross-Predict ResNet"). This cross-prediction baseline measures the shared spatial component: any predictive power it achieves reflects information that is inherently common to both surveys and therefore accessible to either encoder by construction. We find that predictions from physics latents are always worse than the cross-predict baseline, verifying that the physics latent space is not capturing private instrument information. The full results are shown in Appendix A.5.

The key diagnostic is the asymmetry in the split of properties: the physics latents substantially outperform instrument latents at predicting (mostly) physical properties, whereas the pattern reverses for instrument properties. Notably, our latent spaces often contain less information than the baselines when used for cross-prediction (e.g. predicting physics-related properties from the instrument latents), indicating that the model has actively learned to erase instrument-specific information from the physics space and vice versa. On the other hand, we note that AION-1 embeddings retain sensitivity to instrumental properties, but our instrument latent space outperforms both baselines in predicting instrument-related properties. This highlights the primary advantage of our architecture: by explicitly disentangling the latent factors, we achieve a more efficient separation of physics and instrumental properties than monolithic foundation models.

#### Instrument-independent similarity search and rare-object discovery.

We can also use the learned embeddings from our model to search for nearest neighbors (NNs) in the physics and instrument spaces. In astrophysics, we often look for rare events, such as galaxy mergers or strong lenses in large datasets. By performing an  $L_2$  nearest-neighbor search over the encodings generated by our model for our dataset of  $\sim 103k$  cross-matched galaxies, we demonstrate that querying the physics space retrieves physically similar objects from either survey, whereas querying the instrument space isolates objects with similar noise properties. Fig. 5 (Top) shows an example HSC that is used as a query. A mixture of HSC and Legacy images is found in the top neighbors in the physics space. In fact, the five examples shown could have been found among the top nine NNs, even if we used the Legacy image of that galaxy instead. This demonstrates the ability to perform *instrument-independent similarity search* in physics space.

To further demonstrate the effectiveness of our disentangled physics representation, we also query the physics latent space with objects from a rare class. Fig. 5 (Bottom) shows an example where the query is a known strong gravitational lens. The top eight nearest neighbors successfully retrieve

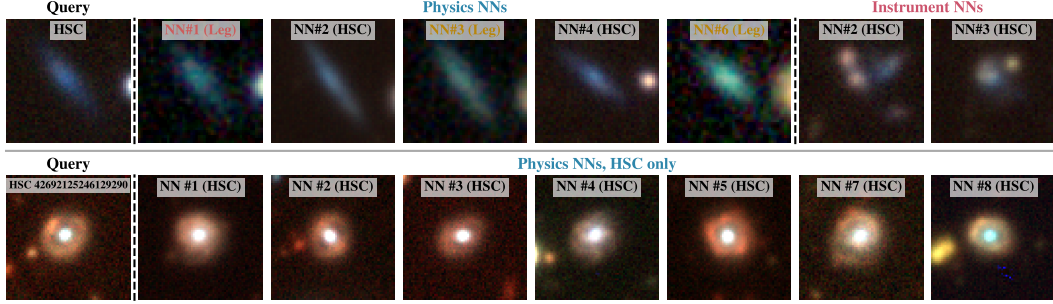


Figure 5: **Instrument-Invariant Search and Rare-Object Discovery.** **Top (Cross-Survey Retrieval):** We search the latent spaces using an HSC observation as query. *Physics Space:* The pair from the alternate survey is identified as the top-1 neighbor, with additional top-ranked neighbors showing physically similar galaxies from a mixture of both instruments. Notably, the four examples shown could have been found within the top nine nearest neighbors independent of which survey the query came from. *Instrument Space:* Neighbors in the instrument space show similar noise characteristics independent of the underlying galactic signal. **Bottom (Strong Lenses):** Nearest neighbor search within the physics latent space using a known strong lens as query, focusing only on the HSC images. The retrieved top neighbors show features suggestive of strong lensing, demonstrating the model’s capacity for rare-object discovery.

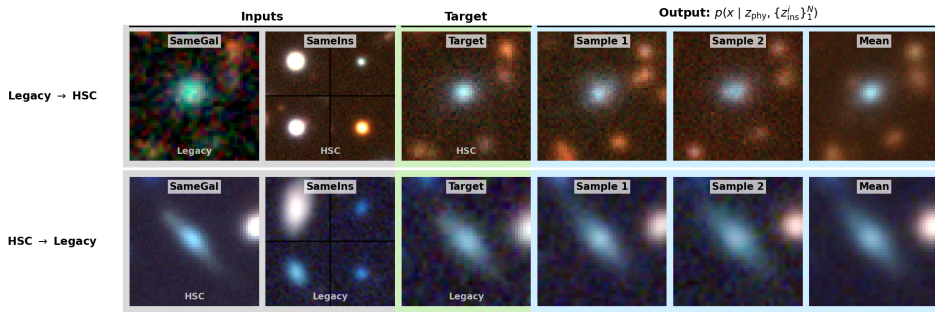


Figure 6: **Cross-instrument Galaxy Reconstructions.** **Columns 1–2 (Inputs):** The target galaxy observed via an alternate instrument (input to the physics encoder) and a set of up to five different galaxies imaged by the target instrument (input to the instrument encoder). **Column 3 (Ground Truth):** The original target image. **Columns 4–5 (Posterior Samples):** Independent samples generated by the decoder, demonstrating the model’s ability to capture noise and uncertainty. **Column 6 (Posterior Mean):** The pixel-wise mean of the generated posterior samples.

multiple HSC images that exhibit strong morphological evidence to be considered candidate lenses. This confirms that the physics latent space effectively isolates and groups complex physical features, streamlining the discovery of rare astrophysical phenomena.

## 4.2 Counterfactual cross-instrument generation.

Fig. 6 shows the model’s ability to reconstruct target observations for both surveys and produce diverse posterior samples that capture the inherent uncertainty in the mapping. In addition to being our training objective, we can use counterfactual generation to prioritize follow-up observations. The discovery of rare objects, such as strong gravitational lenses, often depends critically on image quality. HSC’s higher-resolution allows to resolve features, such as faint arcs, that are blurred or undetected in Legacy imaging. Our model can generate the expected HSC-like appearance for any galaxy in the Legacy footprint, effectively acting as a learned survey simulator that performs instrument-aware super-resolution and denoising. This could enable more targeted follow-up: one could first generate counterfactuals to identify the most promising objects, those where the model predicts lensing features that are plausibly present but partly unresolved in the Legacy data. The actual follow-up observation then provides the real photons needed for confirmation.

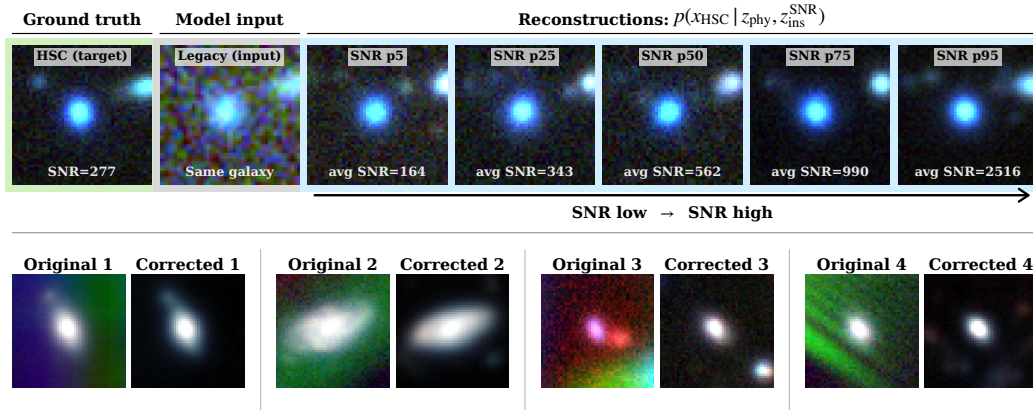


Figure 7: **Data-driven Noise Model. Top (Progressive Denoising):** Reconstructions of a target galaxy from its Legacy counterpart, varying the instrument conditioning across different percentiles of the HSC SNR distribution. The model successfully generates progressively cleaner images; the average SNR shown is that of the images used to condition the reconstruction. **Bottom (Systematic Artifact Removal):** By conditioning the physics encoder on an artifact-corrupted HSC image and the instrument encoder on a random set of HSC images, the model successfully removes severe instrumental distortions while preserving the underlying galaxy morphology.

More broadly, this approach could support population-level studies by extending HSC-like morphological analysis across the full  $20,000 \text{ deg}^2$  Legacy footprint. However, we caution that the model generates the statistically expected appearance given the Legacy input, not a true observation. It can sharpen and denoise features that are marginally detected, but it cannot recover information that is entirely absent from the input. Features well below the Legacy detection threshold will not appear in the counterfactual. The generated images are best understood as informed predictions that reduce the search space for follow-up, rather than replacements for real, deeper observations. To evaluate the generated images, we report MSE computed on the generated images. The posterior samples achieve an MSE of 0.081 for HSC-anchored and 0.197 for Legacy-anchored reconstructions, evaluated over 256 held-out galaxies.

**Zero-shot pipeline transfer.** To further validate that our counterfactual HSC images preserve intrinsic galaxy morphology, we train a ResNet-18 model to predict galaxy ellipticities using 25,000 real HSC images, and apply this frozen model to counterfactual HSC images generated from Legacy observations of held-out galaxies. We found that the predictions match the ground truth with near-identical accuracy for both real ( $R^2 = 0.82$ ) and generated ( $R^2 = 0.81$ ) images. This demonstrates that counterfactually generated images can serve as drop-in replacements for real data, enabling the direct reuse of existing inference pipelines across surveys (Fig. 9, right; Appendix A.6).

**Data-driven noise model.** The instrument encoder and generative decoder together yield a data-driven noise model: by manipulating the instrument conditioning at inference time, we can simulate observations under different conditions while holding the underlying physics fixed. We demonstrate this in two complementary settings (Fig. 7). First, in a *controlled SNR traversal*, we reconstruct an HSC target galaxy from its Legacy counterpart five times, fixing the initial noise sample  $x_0$  but varying the instrument conditioning across the 5th, 25th, 50th, 75th, and 95th percentiles of the HSC SNR distribution (defined as the mean pixel-wise flux divided by the flux error, averaged across channels). Traversing this axis produces progressively cleaner reconstructions, even surpassing the apparent SNR of the ground truth—indicating an exploitable, manipulable noise model rather than memorization. Second, we use this noise model to *remove strong systematics* from real observations: we pass an HSC image corrupted by severe instrumental distortion to the physics encoder and condition the instrument encoder on randomly selected HSC images to specify a baseline noise profile. Crucially, both encoders receive HSC images here (a combination never seen in training) yet the decoder reconstructs the underlying galaxy morphology while removing the artifacts, confirming that the model separates intrinsic physical signals from superimposed sensor distortions.

## 5 Conclusion

We have presented a framework for learning to disentangle instrumental effects from physical signals in scenarios with multiple views of the same object, i.e., observations from different instruments, using a simple counterfactual generative objective. Our dual-encoder architecture separates physics-invariant and instrument-specific factors structurally, without requiring hand-engineered contrastive losses or explicit instrument models. Compared to previous contrastive approaches, our method enables counterfactual generation by synthesizing how a source would appear under different observing conditions, and it is designed to scale to settings with more than two instruments. The generative component can also be viewed as a data-driven instrument model, learned implicitly from cross-matched observations. We have shown an application of our model to galaxy data in astrophysics, showing that the physics latent space recovers physical properties comparably to existing foundation models while being robust to instrument systematics, and that counterfactual generation produces realistic cross-survey translations.

**Limitations and future directions.** Our approach currently requires overlapping observations across instruments, which limits applicability to regions of shared sky coverage. In future work, we aim to extend the framework to unpaired settings where such overlap is unavailable or limited. Moreover, while we have focused on galaxy imaging, the framework is general and applicable to other domains in astrophysics and beyond. In particular, we plan to apply it to the tens of millions of light curves from NASA’s Transiting Exoplanet Survey Satellite [TESS, 22] and Kepler [23, 24] missions.

## Acknowledgments and Disclosure of Funding

This work was supported in part by Advanced Micro Devices, Inc. under the AMD University Program’s AI & HPC Cluster. The project that gave rise to these results received the support of a fellowship from “la Caixa” Foundation (ID 100010434). The fellowship code is B006068. We thank the AstroAI center at the Center for Astrophysics | Harvard & Smithsonian, where P M-P was a summer researcher under the supervision of DM, Rafael Martinez-Galarza, and Cecilia Garraffo, for their support and useful discussions on multimodal foundation models for astronomy. We also thank Michael J. Smith for helping access the dataset, and Rocco Di Tella and Rebeka Bottger for insightful technical discussions.

### Code Availability

A simplified version of the codebase is publicly available.<sup>1</sup> For more information please contact [pablomer@mit.edu](mailto:pablomer@mit.edu).

## References

- [1] J. B. Tenenbaum and W. T. Freeman. Separating style and content with bilinear models. *Neural Computation*, 12:1247 – 1283, 2000.
- [2] Irina Higgins, Loic Matthey, Arka Pal, Christopher Burgess, Xavier Glorot, Matthew Botvinick, Shakir Mohamed, and Alexander Lerchner. beta-VAE: Learning basic visual concepts with a constrained variational framework. In *International Conference on Learning Representations*, 2017. URL <https://openreview.net/forum?id=Sy2fzU9g1>.
- [3] Bernhard Schölkopf, Francesco Locatello, Stefan Bauer, Nan Rosemary Ke, Nal Kalchbrenner, Anirudh Goyal, and Yoshua Bengio. Toward causal representation learning. *Proceedings of the IEEE*, 109(5):612–634, 2021. doi: 10.1109/JPROC.2021.3058954.
- [4] Zeming Lin, Halil Akin, Roshan Rao, Brian Hie, Zhongkai Zhu, Wenting Lu, Nikita Smetanin, Robert Verkuil, Ori Kabeli, Yaniv Shmueli, Allan dos Santos Costa, Maryam Fazel-Zarandi, Tom Sercu, Salvatore Candido, and Alexander Rives. Evolutionary-scale prediction of atomic-level protein structure with a language model. *Science*, 379(6637):1123–1130, 2023. doi: 10.1126/science.ade2574. URL <https://www.science.org/doi/abs/10.1126/science.ade2574>.

---

<sup>1</sup><https://github.com/pablomerc/galaxy-counter.git>

- [5] Jerret Ross, Brian Belgodere, Vijil Chenthamarakshan, Inkit Padhi, Youssef Mroueh, and Payel Das. Large-scale chemical language representations capture molecular structure and properties. *Nature Machine Intelligence*, 4(12):1256–1264, 2022. URL <https://arxiv.org/abs/2106.09553>.
- [6] Yezhen Cong, Samar Khanna, Chenlin Meng, Patrick Liu, Erik Rozi, Yutong He, Marshall Burke, David Lobell, and Stefano Ermon. Satmae: Pre-training transformers for temporal and multi-spectral satellite imagery. *Advances in Neural Information Processing Systems*, 35: 197–211, 2022. URL <https://arxiv.org/abs/2207.08051>.
- [7] Mike Walmsley, Inigo Val Slijepcevic, Micah Bowles, and Anna M. M. Scaife. Towards galaxy foundation models with hybrid contrastive learning, 2022. URL <https://arxiv.org/abs/2206.11927>.
- [8] Liam Parker, Francois Lanusse, Jeff Shen, Ollie Liu, Tom Hehir, Leopoldo Sarra, Lucas Meyer, Micah Bowles, Sebastian Wagner-Carena, Helen Qu, Siavash Golkar, Alberto Bietti, Hatim Bourfoune, Nathan Casserau, Pierre Cornette, Keiya Hirashima, Geraud Krawezik, Ruben Ohana, Nicholas Lourie, Michael McCabe, Rudy Morel, Payel Mukhopadhyay, Mariel Pettee, Bruno Regalado-Saint Blancard, Kyunghyun Cho, Miles Cranmer, and Shirley Ho. Aion-1: Omnimodal foundation model for astronomical sciences. In *The Thirty-ninth Annual Conference on Neural Information Processing Systems*, 2025. URL <https://arxiv.org/abs/2510.17960>.
- [9] The Multimodal Universe Collaboration. The multimodal universe: Enabling large-scale machine learning with 100tb of astronomical scientific data, 2024. URL <https://arxiv.org/abs/2412.02527>.
- [10] Euclid Collaboration, M. Siudek, M. Huertas-Company, M. Smith, G. Martinez-Solaeché, F. Lanusse, S. Ho, E. Angeloudi, P. A. C. Cunha, H. Domínguez Sánchez, M. Dunn, Y. Fu, P. Iglesias-Navarro, J. Junais, J. H. Knapen, B. Laloux, M. Mezcua, W. Roster, G. Stevens, J. Vega-Ferrero, N. Aghanim, B. Altieri, A. Amara, S. Andreon, N. Auricchio, H. Aussel, C. Baccigalupi, M. Baldi, S. Bardelli, P. Battaglia, A. Biviano, A. Bonchi, E. Branchini, M. Brescia, J. Brinchmann, S. Camera, G. Cañas-Herrera, V. Capobianco, C. Carbone, J. Carretero, S. Casas, F. J. Castander, M. Castellano, G. Castignani, S. Cavuoti, K. C. Chambers, A. Cimatti, C. Colodro-Conde, G. Congedo, C. J. Conselice, L. Conversi, Y. Copin, F. Courbin, H. M. Courtois, M. Cropper, A. Da Silva, H. Degaudenzi, G. De Lucia, A. M. Di Giorgio, J. Dinis, C. Dolding, H. Dole, F. Dubath, C. A. J. Duncan, X. Dupac, S. Dusini, S. Escoffier, M. Farina, R. Farinelli, F. Faustini, S. Ferriol, F. Finelli, S. Fotopoulou, M. Frailis, E. Franceschi, S. Galeotta, K. George, B. Gillis, C. Giocoli, J. Gracia-Carpio, B. R. Granett, A. Grazian, F. Grupp, S. Gwyn, S. V. H. Haugan, W. Holmes, I. M. Hook, F. Hormuth, A. Hornstrup, K. Jahnke, M. Jhabvala, E. Kihänen, S. Kermiche, A. Kiessling, B. Kubik, M. Kümmel, M. Kunz, H. Kurki-Suonio, Q. Le Boulc’h, A. M. C. Le Brun, D. Le Mignant, S. Ligorì, P. B. Lilje, V. Lindholm, I. Lloro, G. Mainetti, D. Maino, E. Maiorano, O. Mansutti, S. Marcín, O. Marggraf, M. Martinelli, N. Martinet, F. Marulli, R. Massey, S. Maurogordato, H. J. McCracken, E. Medinaceli, S. Mei, M. Melchior, Y. Mellier, M. Meneghetti, E. Merlin, G. Meylan, A. Mora, M. Moresco, L. Moscardini, R. Nakajima, C. Neissner, S. M. Niemi, J. W. Nightingale, C. Padilla, S. Paltani, F. Pasian, K. Pedersen, W. J. Percival, V. Pettorino, S. Pires, G. Polenta, M. Poncet, L. A. Popa, L. Pozzetti, F. Raison, A. Renzi, J. Rhodes, G. Riccio, E. Romelli, M. Roncarelli, R. Saglia, Z. Sakr, A. G. Sánchez, D. Sapone, B. Sartoris, J. A. Schewtschenko, P. Schneider, T. Schrabback, M. Scodeggio, A. Secroun, G. Seidel, M. Seiffert, S. Serrano, P. Simon, C. Sirignano, G. Sirri, L. Stanco, J. Steinwagner, P. Tallada-Crespí, A. N. Taylor, I. Tereno, S. Toft, R. Toledo-Moreo, F. Torradeflot, I. Tutusaus, L. Valenziano, J. Valiviita, T. Vassallo, G. Verdoes Kleijn, A. Veropalumbo, Y. Wang, J. Weller, A. Zacchei, G. Zamorani, F. M. Zerbi, I. A. Zinchenko, E. Zucca, V. Allevalo, M. Ballardini, M. Bolzonella, E. Bozzo, C. Burigana, R. Cabanac, A. Cappi, D. Di Ferdinando, J. A. Escartin Vigo, L. Gabarra, J. Martín-Fleitas, S. Matthew, N. Mauri, R. B. Metcalf, and A. Pezzotta. Euclid Quick Data Release (Q1) Exploring galaxy properties with a multi-modal foundation model. *arXiv e-prints*, art. arXiv:2503.15312, March 2025. doi: 10.48550/arXiv.2503.15312.
- [11] Jeroen Audenaert, Daniel Muthukrishna, Paul F. Gregory, David W. Hogg, and V. Ashley Villar. Causal foundation models: Disentangling physics from instrument properties, 2025. URL <https://arxiv.org/abs/2507.05333>.

- [12] Bernhard Schölkopf, David W. Hogg, Dun Wang, Daniel Foreman-Mackey, Dominik Janzing, Carl-Johann Simon-Gabriel, and Jonas Peters. Modeling confounding by half-sibling regression. *Proceedings of the National Academy of Sciences*, 113(27):7391–7398, 2016. doi: 10.1073/pnas.1511656113. URL <https://www.pnas.org/doi/abs/10.1073/pnas.1511656113>.
- [13] Soichiro Hattori, Daniel Foreman-Mackey, David W. Hogg, Benjamin T. Montet, Ruth Angus, T. A. Pritchard, Jason L. Curtis, and Bernhard Schölkopf. The unpopular Package: A Data-driven Approach to Detrending TESS Full-frame Image Light Curves. *The Astronomical Journal*, 163(6):284, June 2022. doi: 10.3847/1538-3881/ac625a.
- [14] Yaron Lipman, Ricky T. Q. Chen, Heli Ben-Hamu, Maximilian Nickel, and Matt Le. Flow matching for generative modeling, 2023. URL <https://arxiv.org/abs/2210.02747>.
- [15] Arjun Dey, David J. Schlegel, Dustin Lang, Robert Blum, Kaylan Burleigh, Xiaohui Fan, Joseph R. Findlay, Doug Finkbeiner, David Herrera, Stéphanie Juneau, Martin Landriau, Michael Levi, Ian McGreer, Aaron Meisner, Adam D. Myers, John Moustakas, Peter Nugent, Anna Patej, Edward F. Schlafly, Alistair R. Walker, Francisco Valdes, Benjamin A. Weaver, Christophe Yèche, Hu Zou, Xu Zhou, Behzad Abareshi, T. M. C. Abbott, Bela Abolfathi, C. Aguilera, Shadab Alam, Lori Allen, A. Alvarez, James Annis, Behzad Ansarinejad, Marie Aubert, Jacqueline Beechert, Eric F. Bell, Segev Y. BenZvi, Florian Beutler, Richard M. Bielby, Adam S. Bolton, César Briceño, Elizabeth J. Buckley-Geer, Karen Butler, Annalisa Calamida, Raymond G. Carlberg, Paul Carter, Ricard Casas, Francisco J. Castander, Yumi Choi, Johan Comparat, Elena Cukanovaite, Timothée Delubac, Kaitlin DeVries, Sharmila Dey, Govinda Dhungana, Mark Dickinson, Zhejie Ding, John B. Donaldson, Yutong Duan, Christopher J. Duckworth, Sarah Eftekharzadeh, Daniel J. Eisenstein, Thomas Etourneau, Parker A. Fagrelus, Jay Farihi, Mike Fitzpatrick, Andreu Font-Ribera, Leah Fulmer, Boris T. Gänsicke, Enrique Gaztanaga, Koshy George, David W. Gerdes, Satya Gontcho A Gontcho, Claudio Gorgoni, Gregory Green, Julien Guy, Diane Harmer, M. Hernandez, Klaus Honscheid, Lijuan (Wendy) Huang, David J. James, Buell T. Jannuzi, Linhua Jiang, Richard Joyce, Armin Karcher, Sonia Karkar, Robert Kehoe, Jean-Paul Kneib, Andrea Kueter-Young, Ting-Wen Lan, Tod R. Lauer, Laurent Le Guillou, Auguste Le Van Suu, Jae Hyeon Lee, Michael Lesser, Laurence Perreault Levasseur, Ting S. Li, Justin L. Mann, Robert Marshall, C. E. Martínez-Vázquez, Paul Martini, Hélión du Mas des Bourboux, Sean McManus, Tobias Gabriel Meier, Brice Ménard, Nigel Metcalfe, Andrea Muñoz-Gutiérrez, Joan Najita, Kevin Napier, Gautham Narayan, Jeffrey A. Newman, Jundan Nie, Brian Nord, Dara J. Norman, Knut A. G. Olsen, Anthony Paat, Nathalie Palanque-Delabrouille, Xiyan Peng, Claire L. Poppett, Megan R. Poremba, Abhishek Prakash, David Rabinowitz, Anand Raichoor, Mehdi Rezaie, A. N. Robertson, Natalie A. Roe, Ashley J. Ross, Nicholas P. Ross, Gregory Rudnick, Sasha Gaines, Abhijit Saha, F. Javier Sánchez, Elodie Savary, Heidi Schweiker, Adam Scott, Hee-Jong Seo, Huanyuan Shan, David R. Silva, Zachary Slepian, Christian Soto, David Sprayberry, Ryan Staten, Coley M. Stillman, Robert J. Stupak, David L. Summers, Suk Sien Tie, H. Tirado, Mariana Vargas-Magaña, A. Katherina Vivas, Risa H. Wechsler, Doug Williams, Jinyi Yang, Qian Yang, Tolga Yapici, Dennis Zaritsky, A. Zenteno, Kai Zhang, Tianmeng Zhang, Rongpu Zhou, and Zhimin Zhou. Overview of the desi legacy imaging surveys. *The Astronomical Journal*, 157(5):168, April 2019. ISSN 1538-3881. doi: 10.3847/1538-3881/ab089d. URL <http://dx.doi.org/10.3847/1538-3881/ab089d>.
- [16] Hiroaki Aihara, Nobuo Arimoto, Robert Armstrong, Stéphane Arnouts, Neta A Bahcall, Steven Bickerton, James Bosch, Kevin Bundy, Peter L Capak, James H H Chan, Masashi Chiba, Jean Coupon, Eiichi Egami, Motohiro Enoki, Francois Finet, Hiroki Fujimori, Seiji Fujimoto, Hisanori Furusawa, Junko Furusawa, Tomotsugu Goto, Andy Goulding, Johnny P Greco, Jenny E Greene, James E Gunn, Takashi Hamana, Yuichi Harikane, Yasuhiro Hashimoto, Takashi Hattori, Masao Hayashi, Yusuke Hayashi, Krzysztof G Helminiak, Ryo Higuchi, Chiaki Hikage, Paul T P Ho, Bau-Ching Hsieh, Kuiyun Huang, Song Huang, Hiroyuki Ikeda, Masatoshi Imanishi, Akio K Inoue, Kazushi Iwasawa, Ikuru Iwata, Anton T Jaelani, Hung-Yu Jian, Yukiko Kamata, Hiroshi Karoji, Nobunari Kashikawa, Nobuhiko Katayama, Satoshi Kawanomoto, Issha Kayo, Jin Koda, Michitaro Koike, Takashi Kojima, Yutaka Komiyama, Akira Konno, Shintaro Koshida, Yusei Koyama, Haruka Kusakabe, Alexie Leauthaud, Chien-Hsiu Lee, Lihwai Lin, Yen-Ting Lin, Robert H Lupton, Rachel Mandelbaum, Yoshiki Matsuoaka, Elinor Medezinski, Sogo Mineo, Shoken Miyama, Hironao Miyatake, Satoshi Miyazaki, Rieko Momose, Anupreeta

- More, Surhud More, Yuki Moritani, Takashi J Moriya, Tomoki Morokuma, Shiro Mukae, Ryoma Murata, Hitoshi Murayama, Tohru Nagao, Fumiaki Nakata, Mana Niida, Hiroko Niikura, Atsushi J Nishizawa, Yoshiyuki Obuchi, Masamune Oguri, Yukie Oishi, Nobuhiro Okabe, Sakurako Okamoto, Yuki Okura, Yoshiaki Ono, Masato Onodera, Masafusa Onoue, Ken Osato, Masami Ouchi, Paul A Price, Tae-Soo Pyo, Masao Sako, Marcin Sawicki, Takatoshi Shibuya, Kazuhiro Shimasaku, Atsushi Shimono, Masato Shirasaki, John D Silverman, Melanie Simet, Joshua Speagle, David N Spergel, Michael A Strauss, Yuma Sugahara, Naoshi Sugiyama, Yasushi Suto, Sherry H Suyu, Nao Suzuki, Philip J Tait, Masahiro Takada, Tadafumi Takata, Naoyuki Tamura, Manobu M Tanaka, Masaomi Tanaka, Masayuki Tanaka, Yoko Tanaka, Tsuyoshi Terai, Yuichi Terashima, Yoshiki Toba, Nozomu Tominaga, Jun Toshikawa, Edwin L Turner, Tomohisa Uchida, Hisakazu Uchiyama, Keiichi Umetsu, Fumihiro Uraguchi, Yuji Urata, Tomonori Usuda, Yousuke Utsumi, Shiang-Yu Wang, Wei-Hao Wang, Kenneth C Wong, Kiyoto Yabe, Yoshihiko Yamada, Hitomi Yamanoi, Naoki Yasuda, Sherry Yeh, Atsunori Yonehara, and Suraphong Yuma. The hyper supprime-cam ssp survey: Overview and survey design. *Publications of the Astronomical Society of Japan*, 70(SP1), September 2017. ISSN 2053-051X. doi: 10.1093/pasj/psx066. URL <http://dx.doi.org/10.1093/pasj/psx066>.
- [17] Kaiming He, Xiangyu Zhang, Shaoqing Ren, and Jian Sun. Deep residual learning for image recognition, 2015. URL <https://arxiv.org/abs/1512.03385>.
- [18] Patrick von Platen, Suraj Patil, Anton Lozhkov, Pedro Cuenca, Nathan Lambert, Kashif Rasul, Mishig Davaadorj, Dhruv Nair, Sayak Paul, William Berman, Yiyi Xu, Steven Liu, and Thomas Wolf. Diffusers: State-of-the-art diffusion models. <https://github.com/huggingface/diffusers>, 2022.
- [19] Leland McInnes, John Healy, and James Melville. Umap: Uniform manifold approximation and projection for dimension reduction, 2020. URL <https://arxiv.org/abs/1802.03426>.
- [20] ChangHoon Hahn, K. J. Kwon, Rita Tojeiro, Malgorzata Siudek, Rebecca E. A. Canning, Mar Mezcuca, Jeremy L. Tinker, David Brooks, Peter Doel, Kevin Fanning, Enrique Gaztañaga, Robert Kehoe, Martin Landriau, Aaron Meisner, John Moustakas, Claire Poppett, Gregory Tarle, Benjamin Weiner, and Hu Zou. The DESI PRObabilistic Value-added Bright Galaxy Survey (PROVABGS) Mock Challenge. *The Astrophysical Journal*, 945(1):16, March 2023. doi: 10.3847/1538-4357/ac8983.
- [21] Andrew M. Saxe, Pang Wei Koh, Zhenghao Chen, Maneesh Bhand, Bipin Suresh, and Andrew Y. Ng. On random weights and unsupervised feature learning. In *Proceedings of the 28th International Conference on International Conference on Machine Learning*, ICML'11, page 1089–1096, Madison, WI, USA, 2011. Omnipress. ISBN 9781450306195.
- [22] George R. Ricker, Joshua N. Winn, Roland Vanderspek, David W. Latham, Gáspár Á. Bakos, Jacob L. Bean, Zachory K. Berta-Thompson, Timothy M. Brown, Lars Buchhave, Nathaniel R. Butler, R. Paul Butler, William J. Chaplin, David Charbonneau, Jørgen Christensen-Dalsgaard, Mark Clampin, Drake Deming, John Doty, Nathan De Lee, Courtney Dressing, Edward W. Dunham, Michael Endl, Francois Fressin, Jian Ge, Thomas Henning, Matthew J. Holman, Andrew W. Howard, Shigeru Ida, Jon M. Jenkins, Garrett Jernigan, John Asher Johnson, Lisa Kaltenegger, Nobuyuki Kawai, Hans Kjeldsen, Gregory Laughlin, Alan M. Levine, Douglas Lin, Jack J. Lissauer, Phillip MacQueen, Geoffrey Marcy, Peter R. McCullough, Timothy D. Morton, Norio Narita, Martin Paegert, Enric Palle, Francesco Pepe, Joshua Pepper, Andreas Quirrenbach, Stephen A. Rinehart, Dimitar Sasselov, Bun'ei Sato, Sara Seager, Alessandro Sozzetti, Keivan G. Stassun, Peter Sullivan, Andrew Szentgyorgyi, Guillermo Torres, Stephane Udry, and Joel Villaseñor. Transiting Exoplanet Survey Satellite (TESS). *Journal of Astronomical Telescopes, Instruments, and Systems*, 1:014003, January 2015. doi: 10.1117/1.JATIS.1.1.014003.
- [23] William J. Borucki, David Koch, Gibor Basri, Natalie Batalha, Timothy Brown, Douglas Caldwell, John Caldwell, Jørgen Christensen-Dalsgaard, William D. Cochran, Edna DeVore, Edward W. Dunham, Andrea K. Dupree, Thomas N. Gautier, John C. Geary, Ronald Gilliland, Alan Gould, Steve B. Howell, Jon M. Jenkins, Yoji Kondo, David W. Latham, Geoffrey W. Marcy, Søren Meibom, Hans Kjeldsen, Jack J. Lissauer, David G. Monet, David Morrison, Dimitar Sasselov, Jill Tarter, Alan Boss, Don Brownlee, Toby Owen, Derek Buzasi, David Charbonneau, Laurance Doyle, Jonathan Fortney, Eric B. Ford, Matthew J. Holman, Sara

- Seager, Jason H. Steffen, William F. Welsh, Jason Rowe, Howard Anderson, Lars Buchhave, David Ciardi, Lucianne Walkowicz, William Sherry, Elliott Horch, Howard Isaacson, Mark E. Everett, Debra Fischer, Guillermo Torres, John Asher Johnson, Michael Endl, Phillip MacQueen, Stephen T. Bryson, Jessie Dotson, Michael Haas, Jeffrey Kolodziejczak, Jeffrey Van Cleve, Hema Chandrasekaran, Joseph D. Twicken, Elisa V. Quintana, Bruce D. Clarke, Christopher Allen, Jie Li, Haley Wu, Peter Tenenbaum, Ekaterina Verner, Frederick Bruhweiler, Jason Barnes, and Andrej Prsa. Kepler Planet-Detection Mission: Introduction and First Results. *Science*, 327(5968):977, February 2010. doi: 10.1126/science.1185402.
- [24] David G. Koch, William J. Borucki, Gibor Basri, Natalie M. Batalha, Timothy M. Brown, Douglas Caldwell, Jørgen Christensen-Dalsgaard, William D. Cochran, Edna DeVore, Edward W. Dunham, III Gautier, Thomas N., John C. Geary, Ronald L. Gilliland, Alan Gould, Jon Jenkins, Yoji Kondo, David W. Latham, Jack J. Lissauer, Geoffrey Marcy, David Monet, Dimitar Sasselov, Alan Boss, Donald Brownlee, John Caldwell, Andrea K. Dupree, Steve B. Howell, Hans Kjeldsen, Søren Meibom, David Morrison, Tobias Owen, Harold Reitsema, Jill Tarter, Stephen T. Bryson, Jessie L. Dotson, Paul Gazis, Michael R. Haas, Jeffrey Kolodziejczak, Jason F. Rowe, Jeffrey E. Van Cleve, Christopher Allen, Hema Chandrasekaran, Bruce D. Clarke, Jie Li, Elisa V. Quintana, Peter Tenenbaum, Joseph D. Twicken, and Hayley Wu. Kepler Mission Design, Realized Photometric Performance, and Early Science. *The Astrophysical Journal Letters*, 713(2):L79–L86, April 2010. doi: 10.1088/2041-8205/713/2/L79.
- [25] Hiroaki Aihara, Nobuo Arimoto, Robert Armstrong, Stéphane Arnouts, Neta A. Bahcall, Steven Bickerton, James Bosch, Kevin Bundy, Peter L. Capak, James H. H. Chan, Masashi Chiba, Jean Coupon, Eiichi Egami, Motohiro Enoki, Francois Finet, Hiroki Fujimori, Seiji Fujimoto, Hisanori Furusawa, Junko Furusawa, Tomotsugu Goto, Andy Goulding, Johnny P. Greco, Jenny E. Greene, James E. Gunn, Takashi Hamana, Yuichi Harikane, Yasuhiro Hashimoto, Takashi Hattori, Masao Hayashi, Yusuke Hayashi, Krzysztof G. Helminiak, Ryo Higuchi, Chiaki Hikage, Paul T. P. Ho, Bau-Ching Hsieh, Kuiyun Huang, Song Huang, Hiroyuki Ikeda, Masatoshi Imanishi, Akio K. Inoue, Kazushi Iwasawa, Ikuru Iwata, Anton T. Jaelani, Hung-Yu Jian, Yukiko Kamata, Hiroshi Karoji, Nobunari Kashikawa, Nobuhiko Katayama, Satoshi Kawanomoto, Issha Kayo, Jin Koda, Michitaro Koike, Takashi Kojima, Yutaka Komiyama, Akira Konno, Shintaro Koshida, Yusei Koyama, Haruka Kusakabe, Alexie Leauthaud, Chien-Hsiu Lee, Lihwai Lin, Yen-Ting Lin, Robert H. Lupton, Rachel Mandelbaum, Yoshiki Matsuoka, Elinor Medezinski, Sogo Mineo, Shoken Miyama, Hironao Miyatake, Satoshi Miyazaki, Rieko Momose, Anupreeta More, Surhud More, Yuki Moritani, Takashi J. Moriya, Tomoki Morokuma, Shiro Mukae, Ryoma Murata, Hitoshi Murayama, Tohru Nagao, Fumiaki Nakata, Mana Nida, Hiroko Niikura, Atsushi J. Nishizawa, Yoshiyuki Obuchi, Masamune Oguri, Yukie Oishi, Nobuhiro Okabe, Sakurako Okamoto, Yuki Okura, Yoshiaki Ono, Masato Onodera, Masafusa Onoue, Ken Osato, Masami Ouchi, Paul A. Price, Tae-Soo Pyo, Masao Sako, Marcín Sawicki, Takatoshi Shibuya, Kazuhiro Shimasaku, Atsushi Shimono, Masato Shirasaki, John D. Silverman, Melanie Simet, Joshua Speagle, David N. Spergel, Michael A. Strauss, Yuma Sugahara, Naoshi Sugiyama, Yasushi Suto, Sherry H. Suyu, Nao Suzuki, Philip J. Tait, Masahiro Takada, Tadafumi Takata, Naoyuki Tamura, Manobu M. Tanaka, Masaomi Tanaka, Masayuki Tanaka, Yoko Tanaka, Tsuyoshi Terai, Yuichi Terashima, Yoshiki Toba, Nozomu Tominaga, Jun Toshikawa, Edwin L. Turner, Tomohisa Uchida, Hisakazu Uchiyama, Keiichi Umetsu, Fumihiko Uraguchi, Yuji Urata, Tomonori Usuda, Yousuke Utsumi, Shiang-Yu Wang, Wei-Hao Wang, Kenneth C. Wong, Kiyoto Yabe, Yoshihiko Yamada, Hitomi Yamanoi, Naoki Yasuda, Sherry Yeh, Atsunori Yonehara, and Suraphong Yuma. The Hyper Suprime-Cam SSP Survey: Overview and survey design. *Publications of the Astronomical Society of Japan*, 70:S4, January 2018. doi: 10.1093/pasj/psx066.
- [26] Arjun Dey, David J. Schlegel, Dustin Lang, Robert Blum, Kaylan Burleigh, Xiaohui Fan, Joseph R. Findlay, Doug Finkbeiner, David Herrera, Stéphanie Juneau, Martin Landriau, Michael Levi, Ian McGreer, Aaron Meisner, Adam D. Myers, John Moustakas, Peter Nugent, Anna Patej, Edward F. Schlafly, Alistair R. Walker, Francisco Valdes, Benjamin A. Weaver, Christophe Yèche, Hu Zou, Xu Zhou, Behzad Abareshi, T. M. C. Abbott, Bela Abolfathi, C. Aguilera, Shadab Alam, Lori Allen, A. Alvarez, James Annis, Behzad Ansarinejad, Marie Aubert, Jacqueline Beechert, Eric F. Bell, Segev Y. BenZvi, Florian Beutler, Richard M. Bielby, Adam S. Bolton, César Briceño, Elizabeth J. Buckley-Geer, Karen Butler, Annalisa Calamida, Raymond G. Carlberg, Paul Carter, Ricard Casas, Francisco J. Castander, Yumi Choi, Johan

Comparat, Elena Cukanovaite, Timothée Delubac, Kaitlin DeVries, Sharmila Dey, Govinda Dhungana, Mark Dickinson, Zhejie Ding, John B. Donaldson, Yutong Duan, Christopher J. Duckworth, Sarah Eftekharzadeh, Daniel J. Eisenstein, Thomas Etourneau, Parker A. Fagrelus, Jay Farihi, Mike Fitzpatrick, Andreu Font-Ribera, Leah Fulmer, Boris T. Gänsicke, Enrique Gaztanaga, Koshy George, David W. Gerdes, Satya Gontcho A. Gontcho, Claudio Gorgoni, Gregory Green, Julien Guy, Diane Harmer, M. Hernandez, Klaus Honscheid, Lijuan Wendy Huang, David J. James, Buell T. Jannuzi, Linhua Jiang, Richard Joyce, Armin Karcher, Sonia Karkar, Robert Kehoe, Jean-Paul Kneib, Andrea Kueter-Young, Ting-Wen Lan, Tod R. Lauer, Laurent Le Guillou, Auguste Le Van Suu, Jae Hyeon Lee, Michael Lesser, Laurence Perreault Levasseur, Ting S. Li, Justin L. Mann, Robert Marshall, C. E. Martínez-Vázquez, Paul Martini, Hélión du Mas des Bourboux, Sean McManus, Tobias Gabriel Meier, Brice Ménard, Nigel Metcalfe, Andrea Muñoz-Gutiérrez, Joan Najita, Kevin Napier, Gautham Narayan, Jeffrey A. Newman, Jundan Nie, Brian Nord, Dara J. Norman, Knut A. G. Olsen, Anthony Paat, Nathalie Palanque-Delabrouille, Xiyan Peng, Claire L. Poppett, Megan R. Poremba, Abhishek Prakash, David Rabinowitz, Anand Raichoor, Mehdi Rezaie, A. N. Robertson, Natalie A. Roe, Ashley J. Ross, Nicholas P. Ross, Gregory Rudnick, Sasha Safonova, Abhijit Saha, F. Javier Sánchez, Elodie Savary, Heidi Schweiker, Adam Scott, Hee-Jong Seo, Huanyuan Shan, David R. Silva, Zachary Slepian, Christian Soto, David Sprayberry, Ryan Staten, Coley M. Stillman, Robert J. Stupak, David L. Summers, Suk Sien Tie, H. Tirado, Mariana Vargas-Magaña, A. Katherina Vivas, Risa H. Wechsler, Doug Williams, Jinyi Yang, Qian Yang, Tolga Yapici, Dennis Zaritsky, A. Zenteno, Kai Zhang, Tianmeng Zhang, Rongpu Zhou, and Zhimin Zhou. Overview of the DESI Legacy Imaging Surveys. *The Astronomical Journal*, 157(5):168, May 2019. doi: 10.3847/1538-3881/ab089d.

- [27] François Lanusse, Liam Parker, Siavash Golkar, Miles Cranmer, Alberto Bietti, Michael Eickenberg, Geraud Krawezik, Michael McCabe, Ruben Ohana, Mariel Pettee, Bruno Régaldou-Saint Blancard, Tiberiu Tesileanu, Kyunghyun Cho, and Shirley Ho. AstroCLIP: Cross-modal pre-training for astronomical foundation models. *arXiv preprint arXiv:2310.03024*, 2023.
- [28] Conor Durkan, Artur Bekasov, Iain Murray, and George Papamakarios. Neural spline flows. In *Advances in Neural Information Processing Systems*, volume 32, 2019.
- [29] François Rozet, Felix Andry, François Lanusse, and Gilles Louppe. Zuko: Normalizing flows in PyTorch, 2023. URL <https://github.com/probabilists/zuko>.

## A Appendix

### A.1 Model Architecture

We use a ResNet-18 [17] architecture for the encoders, plus a UNet2DConditionModel [18] for the flow-matching generative decoder. The final pooling and projection layers of the ResNet are replaced with a convolution that produces a  $2 \times 2$  feature map with 16 channels, which is treated as a sequence of 4 tokens of size 16 and passed to the UNet via attention conditioning (matching the cross-attention dimension of 16). Table 1 shows the architecture parameters used in the final training run.

Table 1: Model architecture parameters for the conditional flow matching model with dual ResNet-18 encoders.

Parameter	Value
<i>Data Dimensions</i>	
Image size	$48 \times 48$
Input channels	4
Conditioning channels	4
<i>UNet Architecture</i>	
Base model channels	128
Channel multiplier	(1, 2, 4, 4)
Layers per block	2
Attention head dimension	8
Cross-attention dimension	16
Block types (down/up)	CrossAttnDownBlock2D / CrossAttnUpBlock2D
<i>Encoder Architecture</i>	
Backbone	ResNet-18 (timm)
Pretrained weights	False
Projection layer	Replaced by Conv2d(512 $\rightarrow$ 16, kernel=1)

### A.2 Training Configuration

The model was trained using distributed data parallel across 4 NVIDIA H100 GPUs with *bfloat16* mixed precision, completing 75,000 training steps in approximately 8 hours of wall-clock time. Table 2 shows the training configuration and hyperparameters used in the final training run.

Table 2: Training configuration and hyperparameters.

Parameter	Value
<i>Optimization</i>	
Optimizer	AdamW
Learning rate	$1 \times 10^{-4}$
LR scheduler	CosineAnnealingLR
Loss function	Velocity MSE
<i>Flow Matching</i>	
Integration steps (sampling)	250
Interpolation	$x_t = (1 - t)x_0 + tx_1$
Target velocity	$v(x_t, t, c) = x_1 - x_0$
<i>Training Details</i>	
Batch size	64
Total training steps	75,000
Number of devices	4 (DDP)
Precision	bf16-mixed
Validation check interval	Every 1,000 steps
Train/val split ratio	95% / 5%

### A.3 Model Used to Evaluate Downstream Performance

To evaluate the information content of our disentangled latent spaces, we perform supervised regression on a variety of physical and instrumental properties. We use a three-layer Multi-Layer Perceptron (MLP) with hidden dimensions of [512, 256, 128], employing LayerNorm, GELU activations, and 20% dropout. The models are optimized using a Smooth L1 loss to ensure robustness against outliers in the catalog labels.

### A.4 Galaxy Properties Used for Downstream Task

**Dataset Composition.** All downstream-task evaluations are conducted on a single cross-matched sample of  $n = 5,469$  paired galaxies. The MLP probe is trained on a random 90% split of this sample and evaluated on the held-out 10%.

For the subset of physical properties that require DESI BGS spectroscopy (redshift  $z$ ,  $\log M_*$ , sSFR, mass-weighted stellar age  $t_{\text{age}}$  and mass-weighted metallicity  $\log Z_{\text{Met}}$ , all taken from the PROVABGS posterior catalogue), we drop the  $\sim 800$  rows where the spectroscopic label is missing, leaving  $n_{\text{spec}} = 4,666$  galaxies. For every other target — ellipticity components  $e_1, e_2$  (from both the Legacy and HSC shape catalogues), Galactic extinction  $E(B-V)$  on the Legacy side and the HSC extinction  $a$  (cross-matched in from the HSC catalogue  $a_*$  columns), as well as the instrumental metadata (PSF size, PSF depth, galaxy depth and observation count) — the full  $n_{\text{tot}} = 5,469$  sample is used. See below for a more in-depth description of the individual properties.

**Physical properties.** Table 3 summarizes the physical parameters used to evaluate the physics latent space. These span a range of galaxy properties: morphological quantities (ellipticity and half-light radius) measured directly from HSC imaging, spectroscopic redshift from DESI, and stellar population properties (stellar mass, specific star formation rate, metallicity, and stellar age) derived from Bayesian SED fitting by PROVABGS [20]. The SED-derived quantities are inferred by jointly fitting stellar population synthesis models to DESI spectra and Legacy Survey photometry, and thus represent indirect measurements that integrate information beyond what is available in broadband imaging alone. Redshift is the most precisely determined of these quantities, as it is measured directly from spectral line positions.

Table 3: Physical parameters used for downstream regression evaluation of the physics latent space.

Variable	Source	Description
Ellipticity ( $e_1, e_2$ )	HSC catalog	Galaxy shape ellipticity components, measured via the SDSS-style second moments of the surface brightness distribution.
Redshift ( $z$ )	DESI spectra	Spectroscopic redshift.
Stellar mass ( $M_*$ )	PROVABGS	Total mass in stars, derived from Bayesian spectral energy distribution (SED) fitting to DESI spectra [20].
Half-light radius ( $R_{\text{eff}}$ )	HSC catalog	Circularised radius enclosing half of the galaxy’s total light. A measure of galaxy size.
sSFR	PROVABGS	Specific star formation rate $\log(\text{SFR}/M_*)$ : the rate at which new stars are forming normalised by the galaxy’s stellar mass.
$\log Z_{\text{Met}}$	PROVABGS	Gas-phase metallicity: the abundance of elements heavier than helium in the galaxy’s gas. Traces the galaxy’s chemical enrichment history.
$t_{\text{age}}$	PROVABGS	Mass-weighted stellar population age: the average age of the stars in the galaxy.

**Instrumental properties.** Table 4 summarizes the instrumental and observational parameters used to evaluate the instrument latent space. These quantities describe the local observing conditions at each galaxy’s position and vary spatially across each survey’s footprint. For the Legacy Survey, the catalog provides direct measurements of depth (both for point sources and extended galaxies), PSF size, number of contributing exposures, and foreground dust extinction. HSC provides analogous

quantities for PSF size and dust extinction, though computed differently as noted below. We evaluate the instrument latent space on properties from both surveys to assess whether the encoder captures instrument-specific conditions for the survey it is given, without encoding information from the other survey.

Table 4: Instrumental and observational parameters used for downstream regression evaluation of the instrument latent space. All quantities vary spatially across each survey’s footprint.

Variable	Bands	Description
<i>HSC (Hyper Suprime-Cam)</i>		
psf_fwhm	$g, i, r, z$	Effective size of the point spread function (arcsec): how much the instrument and atmosphere spread the light from a point source. Analogous to Legacy PSFSIZE. <sup>†</sup>
a	$g, i, r, z$	Milky Way dust extinction $A_\lambda$ per band (mag). Equivalent to Legacy EBV scaled by a filter-dependent coefficient: $A_\lambda = R_\lambda E(B - V)$ . <sup>‡</sup>
<i>Legacy Survey (DESI Legacy Imaging Surveys)</i>		
NOBS	$g, i, r, z$	Number of exposures contributing to the coadd.
GALDEPTH	$g, i, r, z$	$5\sigma$ detection depth for a round exponential galaxy with $r_e = 0.45''$ (mag). Shallower than PSFDEPTH because galaxy flux is spread over more pixels.
PSFDEPTH	$g, i, r, z$	$5\sigma$ detection depth for a point source (mag).
PSFSIZE	$g, i, r, z$	Effective PSF size (arcsec). See HSC psf_fwhm above. <sup>†</sup>
EBV	—	Milky Way dust extinction as colour excess $E(B - V)$ (mag). See HSC a above. <sup>‡</sup>

<sup>†</sup> Both quantities measure how much the instrument and atmosphere spread the light from a point source, but are computed differently: HSC derives it from the second moments of the coadd PSF model at each source position [25]; the Legacy Survey reports the exposure-weighted mean of the per-CCD PSF FWHM [26].

<sup>‡</sup> Both are derived from the same Milky Way dust maps. Galactic extinction is a foreground astrophysical effect that depends on sky position, not on the instrument; it is included here because it modifies the observed flux analogously to an instrument systematic.

## A.5 Downstream Task Results

Table 5 reports the full set of MLP-probe  $R^2$  scores on the held-out *overlap*-MMU sample, expanding on the summary in Fig. 4. We probe four representations: our physics latents (flattened across tokens), our instrument latents (mean-pooled across tokens), AION-1 (Base) embeddings [8], and a frozen randomly initialized ResNet-18 with the same architecture as our encoders. For instrument properties only, we additionally include a *cross-predict* baseline: a ResNet-18 trained from scratch to predict each survey’s instrument properties from the *other* survey’s raw image. The two right-most columns are external reference values from the literature and are not compared against the other entries.

The physics latent space matches AION-1 within a few percentage points on most physics-related targets, despite using a much smaller latent dimension. The instrument latent space dominates on instrument-related properties, while the physics latents collapse near the random-baseline level on those same properties — consistent with the disentanglement reported in the main text. The cross-predict baseline outperforms our instrument latents only on extinction-like quantities, where information about the other survey’s footprint is sufficient to recover the target.

**The role of spatial-neighbor pairing.** Recall that the instrument encoder is conditioned on the five nearest spatial neighbors of the anchor within the same survey, motivated by the fact that nearby observations share similar instrument conditions. To validate this choice, we train an ablation variant in which the five conditioning galaxies are drawn at random instead. The instrument latent’s recovery of instrument properties collapses (e.g.  $R^2$  on Galaxy Depth drops from 0.68 to 0.20, and on # Observations from 0.50 to nearly 0), while physics-target performance changes only modestly. This confirms that spatially-close pairing supplies the training signal driving instrument-

Table 5: MLP-probe  $R^2$  on the held-out *overlap*-MMU sample. **Bold** = best in row among the five probe methods (the two right-most columns are literature reference values and are not compared against). ‘Ours (Physics)’ and ‘Ours (Instrument)’ use our flow-matching encoder’s  $e_1$  (flat) and  $e_2$  (mean-pooled) latents respectively. ‘AION-1 (Base)’ is the AION-1 Base model [8] probed identically. ‘Rand. Init. ResNet’ is a frozen randomly-initialised ResNet-18 of the same architecture as our encoders. ‘Cross-predict’ is a fresh ResNet-18 trained from scratch to predict each survey’s instrument properties from the *other* survey’s raw image (only defined for instrument targets). Reference values: AION-1-B (Ph+Im) from [8] Table 1; AstroCLIP image-only on Legacy  $\{g, r, z\}$  from [27]. Band-averaged where applicable.

Property	Probe on cross-matched Legacy-HSC sample (Im)					Literature Reported Values	
	Ours (Phys)	Ours (Instr)	AION-1-B	Rnd In. ResNet	X-Predict	AION-1-B (Ph+Im)	AstroCLIP (Im)
<i>Phys.-related properties</i>							
Ellipticity $e_2$	0.934	0.321	<b>0.941</b>	0.616	—	—	—
Ellipticity $e_1$	0.918	0.421	<b>0.939</b>	0.613	—	—	—
Redshift $z$	0.801	0.535	<b>0.857</b>	0.514	—	0.930	0.780
$\log M_*$	0.755	0.491	<b>0.818</b>	0.485	—	0.890	0.730
sSFR	0.558	0.297	<b>0.624</b>	0.312	—	0.640	0.420
$t_{\text{age}}$	0.257	0.114	<b>0.353</b>	0.091	—	0.450	0.290
$\log Z_{\text{Met}}$	0.250	0.155	<b>0.276</b>	0.123	—	0.490	0.360
<i>Legacy Ins. Properties</i>							
Galaxy Depth	0.185	<b>0.682</b>	0.426	0.202	0.214	—	—
PSF Depth	0.181	<b>0.667</b>	0.409	0.191	0.210	—	—
PSF size	0.284	<b>0.556</b>	0.290	0.111	0.313	—	—
Extinction $E(B-V)$	0.159	0.551	0.326	0.232	<b>0.648</b>	—	—
# Observations	0.074	<b>0.501</b>	0.166	0.073	0.197	—	—
<i>HSC Ins. Properties</i>							
Extinction $a$	0.114	0.546	0.299	0.204	<b>0.669</b>	—	—
PSF size	0.069	<b>0.438</b>	0.097	0.021	0.368	—	—

side disentanglement: random pairs do not present consistent enough instrument conditions for the model to separate them from physics.

## A.6 Generative Model Evaluation

We assess the counterfactual generative decoder along three complementary axes: (1) preservation of spatial structure across scales, (2) calibration of the pixel-wise posterior, and (3) preservation of intrinsic galaxy morphology under pipeline transfer (the last is presented in the main text; see also Fig. 9, right). All evaluations use a held-out test set, with 32 posterior samples generated per anchor.

**Spatial structure preservation.** To test that the generated images preserve realistic spatial structure and correlation patterns, we compute the power spectral density (PSD) and pixel-lag autocorrelation for each of the four imaging bands, in both reconstruction directions (Legacy→HSC and HSC→Legacy). Fig. 8 shows strong agreement between ground truth and generated samples across spatial scales for both directions, indicating that the model reproduces realistic galaxy morphologies and instrument noise characteristics rather than pixel-level artifacts (which would manifest as excess high-frequency power) or overly-smoothed outputs (which would appear as a deficit). The posterior uncertainty bands (shaded regions) appropriately expand at higher spatial frequencies, where noise dominates.

**Pixel-wise posterior calibration.** We further validate the uncertainty calibration of the flow-matching posterior using the pixel-wise Z-score,

$$Z = \frac{x - \mathbb{E}[\hat{x}]}{\text{std}(\hat{x})},$$

where  $x$  is the ground-truth pixel value and  $\mathbb{E}[\hat{x}]$ ,  $\text{std}(\hat{x})$  are the posterior mean and standard deviation estimated from the generated samples. Fig. 9 (left) shows that  $Z$  closely follows a standard normal for both survey directions, indicating that the posterior mean is approximately unbiased and the residual uncertainty is approximately Gaussian. The standard deviations slightly above unity indicate mild overconfidence (the model underestimates the true pixel-wise variance by  $\sim 15\%$ ) and the effect is more pronounced for HSC-anchored reconstructions, consistent with the greater ambiguity in generating higher-resolution images from lower-resolution conditioning.

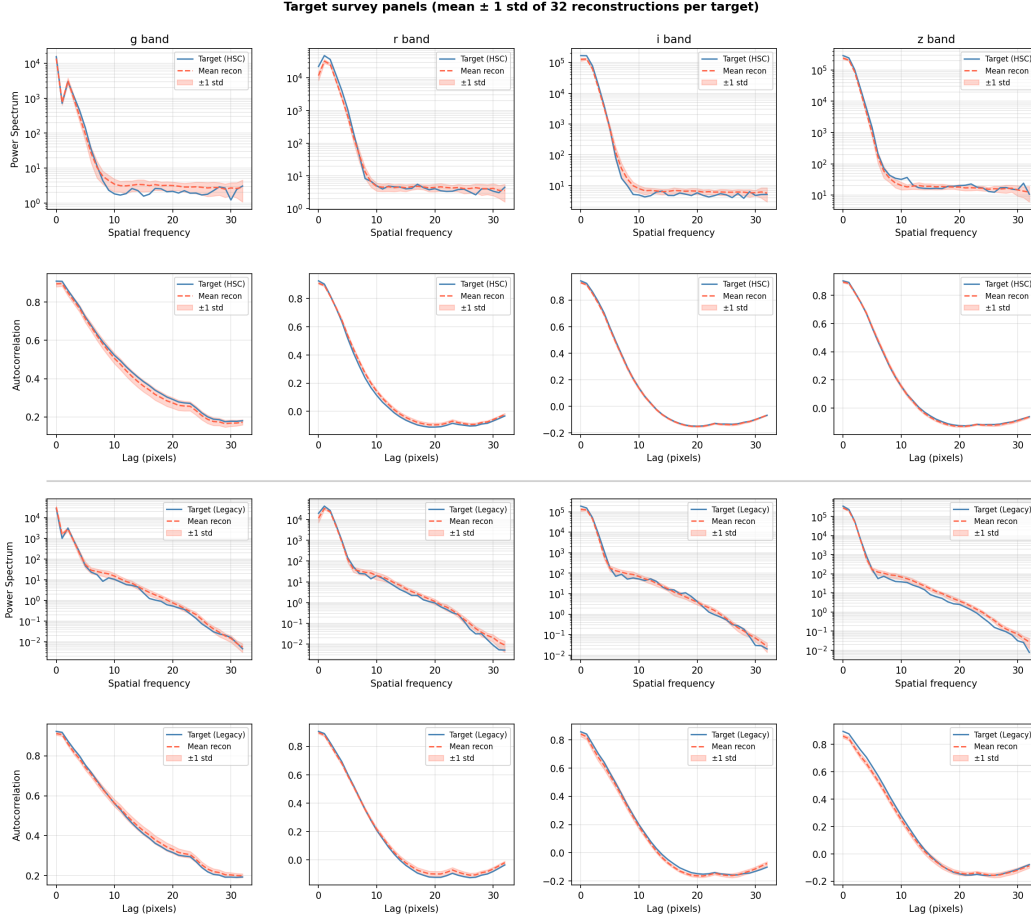


Figure 8: **Spatial Structure Preservation.** Power spectrum (left) and autocorrelation (right) per band for ground-truth and generated images. Each plot shows the true value (blue), the posterior mean from 32 generated samples (orange dashed line), and the  $1\sigma$  posterior standard deviation (orange shaded region). Strong agreement across spatial frequencies and pixel separation (lag) distances indicates that the model captures realistic morphological structure and noise properties.

### A.7 Normalizing Flow for Outlier Detection

To rank candidate outliers, we fit a normalizing flow to the empirical density of the embeddings in each latent space and use the negative log-likelihood  $-\log p(z)$  as the anomaly score. We use a Neural Spline Flow (NSF; 28) implemented in zuko [29], with 6 coupling transforms and a 2-layer MLP of width 64 in each transform. The flow is unconditional (`context=0`) and is trained by maximum likelihood with Adam.

We use the embeddings from just the HSC images for this experiment. We fit a separate flow for each representation we score: (i) our physics latent flattened across the 4 spatial tokens (64D), (ii) our instrument latent mean-pooled across tokens (16D), and (iii) AION-1 (Base) 768D mean-pooled embedding. For AION-1 we also tried fitting the flow to embeddings reduced to 64D via PCA fit on the training split and obtained qualitatively similar outliers. For each space we use 80% of the  $\sim 100,000$  HSC galaxies to fit the flow and score the full sample under the trained model; the lowest-likelihood examples are the candidate outliers shown in Fig. 3. Table 6 lists the hyperparameters used.

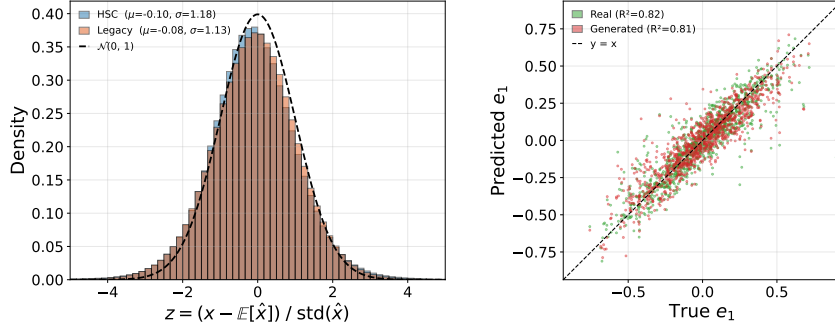


Figure 9: **Left:** Pixel-wise Z-score distribution of generated posterior samples relative to ground-truth target images, across all pixels and held-out galaxies. Both HSC-anchored and Legacy-anchored reconstructions closely approximate a standard normal distribution, indicating that the posterior mean is approximately unbiased, the posterior variance captures the true prediction error, and that the residual uncertainty is approximately Gaussian. The standard deviations slightly above unity indicate mild overconfidence, more pronounced for HSC-anchored reconstructions, consistent with the greater ambiguity in generating higher-resolution images from lower-resolution conditioning. **Right:**  $R^2$  for galaxy ellipticity from a ResNet trained on real HSC images, evaluated on real versus counterfactual HSC images. Near-identical performance shows that existing HSC pipelines can be readily applied to Legacy images through our counterfactual model, extending HSC-quality analysis across the full Legacy footprint.

Table 6: Normalizing flow architecture and training hyperparameters used for outlier detection.

Parameter	Value
<i>Flow Architecture</i>	
Family	Neural Spline Flow (NSF, zuko)
Number of transforms	6
Hidden features per transform	[64, 64]
Context dimension	0 (unconditional)
Input dimension	64 / 16 (Ours) / 768 (AION-1)
<i>Optimization</i>	
Loss	Negative log-likelihood
Optimizer	Adam
Learning rate	$1 \times 10^{-3}$
Batch size	512
Epochs	50
Model selection	Lowest mean training NLL (best-state checkpoint)
<i>Data Split</i>	
Train fraction	80%
Scoring set	All $\sim 100,000$ HSC galaxies
Random seed	42